High-Sensitivity NO2 Gas Sensor: Exploiting UV-Enhanced Recovery in a Hexadecafluorinated Iron Phthalocyanine-Reduced Graphene Oxide

J. Cruz Lozada, K. Kisslinger

To be published in "ACS Omega"

February 2025

Center for Functional Nanomaterials

Brookhaven National Laboratory

U.S. Department of Energy

USDOE Office of Science (SC), Basic Energy Sciences (BES). Scientific User Facilities (SUF)

DISCLAIMER

ACS OMEGA
http://pubs.acs.org/journal/acsodf
Article

High-Sensitivity NO_2 Gas Sensor: Exploiting UV-Enhanced Recovery in a Hexadecafluorinated Iron Phthalocyanine-Reduced Graphene Oxide

John A. Cruz Lozada, Ricardo A. Rosario, Soraya Y. Flores, Kim Kisslinger, Luis F. Fonseca, and Dalice M. Piñero Cruz*

Cite This: *ACS Omega* 2025, 10, 2809−2818

Read Online

ACCESS | Metrics & More | Article Recommendations | Supporting Information

ABSTRACT: Monitoring ultralow nitrogen dioxide (NO_2) concentrations is crucial for air quality management and public health. However, the existing NO_2 gas sensors have several defects, like high cost and power consumption, and exhibit poor selectivity. This study addresses these challenges by presenting a novel hexadecafluorinated iron phthalocyanine-reduced graphene oxide ($FePcF_{16}$-rGO) covalent hybrid sensor for NO_2 detection. This innovative approach, which overcomes the limitations of fabrication cost, energy efficiency, and gas selectivity, is a significant step forward in gas sensor technology. The sensor demonstrates exceptional sensitivity toward ultralow NO_2 concentrations (15.14% response for 100 ppb) with a rapid 60 s UV light-induced recovery. Additionally, the sensor exhibits high selectivity for NO_2, achieving a limit of detection (LOD) of 8.59 ppb. This approach paves the way for developing cost-effective, energy-efficient, and miniature NO_2 monitoring devices for improved environmental monitoring and enhanced safety in workplaces where NO_2 exposure is a concern.

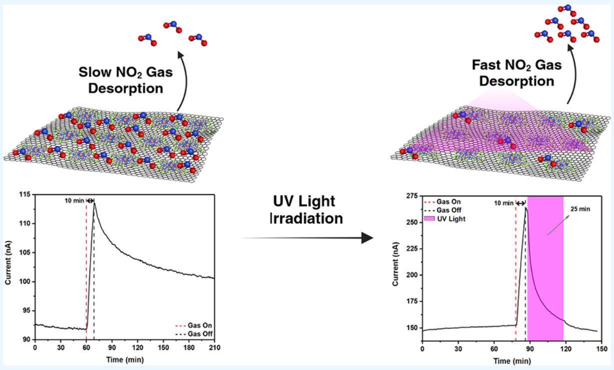

■ INTRODUCTION

Toxic gases are often odorless and colorless; even very low concentrations threaten human health. For this reason, advanced gas sensors are required to trace air pollutants.[1] Although effective, traditional environmental sensors, such as mass spectroscopy, gas chromatography, and Fourier transform infrared spectroscopy, have many drawbacks, such as high energy consumption, bulkiness, complexity in data analysis, and interference due to other gases and humidity.[2] New sensor technologies include electrochemical, acoustic, nondispersive infrared, and organic-based chemiresistive sensors, among others.[3] These new sensor technologies can overcome these deficiencies with enhanced precision and efficiency for air quality monitoring, workplace safety, and medical diagnosis applications.[4,5] The innovations enable the detection of harmful gases, such as nitrogen dioxide (NO_2), cost-effectively and with energy efficiency. NO_2, mainly emitted by fossil fuel combustion, is a toxic pollutant to human health and the environment.[6,7] It leads to severe respiratory disorders due to long-term exposure, even at low part per billion (ppb) levels, and contributes to ozone formation and acid rain.[8−11] Effective NO_2 sensors are required to mitigate the risks. Still, while sensitive, conventional metal oxide semiconductor sensors require high operating temperatures and suffer from power inefficiency, selectivity, and stability.[12−15] Advances in gas sensing technology aim to develop high-performance sensors that can detect NO_2 at room temperature, which is a significant move toward practical and portable devices.

The realization of this critical need has seen the growth of different gas sensing technologies, with each sensing technology trying to solve specific problems that occur with detecting a particular gas. For example, it has been observed that conducting polymer composites, metal−organic frameworks, and carbon-based nanomaterials have great sensitive and versatile performance with a wide range of toxic gas detection.[16−18] Many such materials can work at room temperature, which makes these sensors energy-efficient and suitable for portable applications. However, material and sensor design strongly influence their selectivity to certain gases. For example, Duan et al. prepared a polyaniline (PANI) composite with halloysite nanotubes (HNTs) using a simple in situ polymerization method to enhance the performance of

Received: September 20, 2024
Revised: December 27, 2024
Accepted: December 31, 2024
Published: January 16, 2025

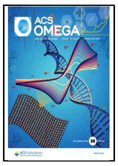

ammonia (NH_3) gas sensing. The PANI/HNTs sensor exhibited enhanced sensitivity, 7.26% ppm^{-1} for 0.1–10 ppm NH_3, a higher response, 91.99% to 10 ppm NH_3, and faster response/recovery times, 158/169 s, which shows how one can optimize a gas sensor for a single toxic gas.[19]

The specific detection of NO_2, a highly adverse and health-threatening pollutant, takes other material considerations into account. NO_2 is chemically reactive and often coexists with other gases, making selectivity and stability critical parameters for sensors. For this reason, recent advances in nanostructured materials, such as transition metal carbides/nitrides, nanoparticles, and graphene-based hybrid materials, have addressed some challenges by offering enhanced selectivity and sensitivity at room temperature.[20,21] For example, transition metal carbides/nitrides have excellent electrical conductivity and chemical stability with a high surface area, which could enable the effective detection of NO_2 through their unique layered structure and abundant active sites.[22] Similarly, graphene-based materials are also very suitable for exceptional sensing due to their high surface-to-volume ratio, robust conductivity, and versatile functionalization possibilities, rendering both materials suitable for NO_2 sensing at room temperature.

Graphene nanosheet-based gas sensors, especially those based on graphene oxide (GO) and reduced graphene oxide (rGO), have emerged as new technologies featuring high specific surface area, chemical stability, and tunable optical and electrical properties.[23,24] Since the pioneering work of Novoselov's group in 2007, showing conductivity changes of graphene upon exposure to gas molecules.[25] rGO has exhibited promising selectivity toward NO_2 and other gases. Other works, such as incorporating rGO into electrospun nylon-6 fibers by Park et al. and the thermal annealing processes by Zhou et al., have reported improved flexibility, stability, and gas sensing performance.[26,27] Hybrid structures, such as rGO/tungsten disulfide (WS_2) heterojunctions, have also exhibited improved room-temperature responses and stability.[28] Nevertheless, several limitations involving rGO-based sensors include solubility, recovery time, and selectivity.[29,30] Functionalization or doping of rGO, especially with materials like metal phthalocyanines (MPs), has efficiently enhanced sensitivity and selectivity.[31] MPcs represent versatile organic semiconductors, having a planar macrocycle structure with a tunable central metal ion that can be adjusted to show p-type or n-type semiconductor behavior in targeted gas detection.[32−34] These structural and electronic properties, combined with MPcs' ability to interact extensively with gas molecules, have been exploited to detect pollutants like NH_3, hydrogen sulfide (H_2S), chlorine (Cl_2), and volatile organic compounds (VOCs).[35−38] For example, Guo et al. reported enhanced sensitivity to NH_3 by hybridizing CoPc with rGO, while Kumar et al. used MPcs with rGO for Cl_2 detection, illustrating the potential of rGO-MPc hybrids for high-performance gas sensing.[39,40]

Recent research in our laboratory has explored the fabrication and application of MPc-based nanowire sensors for gas detection. Otero et al. focused on developing a palladium phthalocyanine nanowire sensor for detecting NO_2 at subppm levels, demonstrating its effectiveness at room temperature with a notable response even at 0.5 ppm.[41] Flores et al. investigated the use of fluorinated iron and cobalt phthalocyanine nanowire sensors for environmental gas monitoring, particularly for detecting NH_3 in the ultralow ppb range, emphasizing their suitability for long-term monitoring in recovery zones due to their low power consumption and room-temperature operation.[35] Inspired by these promising results, we present a novel approach to NO_2 sensing by developing a nanohybrid material based on hexadecafluorinated iron phthalocyanine ($FePcF_{16}$) and rGO. This innovative hybrid structure aims to leverage the synergistic properties of both components to achieve exceptional sensitivity, selectivity, and rapid recovery for NO_2 detection, particularly at low concentrations relevant to environmental monitoring and workplace safety. Moreover, we anticipate that the incorporation of rGO will significantly improve the conductivity of the sensing material, allowing for the fabrication of high-current sensors that offer benefits such as enhanced signal strength and faster response times.

EXPERIMENTAL SECTION

Materials. All chemicals and reagents used in the study were sourced commercially and employed without further purification. Dehydrated N, N-dimethylformamide (DMF), acetone, ethanol, *n*-hexane, and graphite were obtained from Sigma-Aldrich and utilized without additional purification. Tetrafluorophthalonitrile (PnF_4) and iron(II) acetate ($Fe(OAc)_2$) were acquired from Fisher Scientific. GO, $FePcF_{16}$, and $FePcF_{16}$-rGO hybrid were synthesized according to the literature.[31,35,39]

Synthesis of $FePcF_{16}$. A mixture of PnF_4 (500 mg; 2.5 mmol) and $Fe(OAc)_2$ (435 mg; 2.5 mmol) was added in a 25 mL Teflon liner. The Teflon liner was capped inside an argon drybox and placed inside a reactor, then removed and placed inside an oven and heated to 250 °C for 5 h. The reaction was left inside the oven until it reached room temperature; the obtained dark-violet solid was pulverized using a mortar and pestle. The resulting powder was placed in boiling hexane to remove any unreacted phthalonitrile, then filtered and washed with nanopure water to remove unreacted $Fe(OAc)_2$. Afterward, the crude dry powder was extracted for 2 days with a Soxhlet apparatus using dry acetone that gave a blue liquid. The collected liquid was roto evaporated, thus affording a dark-violet solid that was oven-dried at 75 °C.

Preparation of the $FePcF_{16}$-rGO Hybrid. The $FePcF_{16}$-rGO hybrid was prepared by hydrazine reduction of GO in the presence of the $FePcF_{16}$. GO was prepared using a modified Hummer method.[31,39] GO (100 mg) was sonicated in a Schlenk tube in DMF for 2 h to form a homogeneous dispersion. The $FePcF_{16}$ (200 mg) was dissolved in DMF, added dropwise to GO dispersion, and sonicated for 2 h. Afterward, hydrazine and ammonia–water were added. The Schlenk tube containing the resulting mixture was then placed in an oil bath at 100 °C and stirred for 24 h under a nitrogen atmosphere. The solution was cooled and filtered, then washed with DMF, ethanol, and acetone in sequence until the filtrate was colorless. The resulting black powder was transferred into a vial and placed in a vacuum oven at 60 °C for 24 h.

Characterization. UV/vis absorption spectra were recorded using a Shimadzu UV-1800 (Kyoto, Japan). FT-IR was recorded on a Nicolet iS50 (Rochester, NY, USA). The Raman spectra were obtained using a Raman spectrophotometer (HR800, HORIBA JobinYvon Company) exploited by a laser with a 457.9 nm wavelength. The materials' scanning electron microscopy (SEM) images were obtained using a Phenom Pharos G2 Desktop FEG-SEM (Thermo Fisher Scientific Corporation). The transmission electron microscopy (TEM) work was done using a FEI F200X.

Gas Sensor Fabrication and Sensing Measurements. A drop-casting technique was employed to fabricate the gas sensor. This involved preparing a 1.0 mg/mL dispersion of the $FePcF_{16}$-rGO hybrid in ethanol. The mixture was sonicated for 2 h, and then 50 μL was dispersed on top of gold interdigitated electrodes (IDE). The solvent was then evaporated, followed by placing the sensor in a vacuum oven for 5 h at 80 °C to remove residual solvent. The same procedure was applied to the rGO and $FePcF_{16}$ gas sensors.

The gas sensor testing procedure, adapted from a previously published protocol by our laboratory, involved placing the prepared sensor in an MMR Technologies LTMP gas testing chamber, electrically connecting it with tungsten tips, and testing it at room temperature (24 ± 1 °C) using a Keithley 6487 Picoammeter/Voltage Source to record current every 15 s, while exposing it to controlled nitrogen and NO_2 mixture, regulated by MKS GE50A Mass Flow Controllers at a total flow rate of 500 sccm and monitored by an MKS 946 Vacuum System Controller.[35]

Equations 1 and 2 were used to characterize the gas sensor's response at room temperature (RT) and its ability to recover to its initial state upon gas exposure and removal:[42]

$$\text{response}\ (\%) = \frac{I_g - I_0}{I_0} \times 100\% \tag{1}$$

$$\text{recovery}\ (\%) = \frac{I_g - I_r}{I_g - I_0} \times 100\% \tag{2}$$

where I_0 is the initial current intensity before the exposure to the pollutant gas, I_g is the current upon exposure to the pollutant gas at a certain time "*t*", and I_r is the recovery current at a specific time. The light source in the experiment was a UV light-emitting diode (LED) with a wavelength of 365 nm and a power output of 18.4 W.

■ RESULTS AND DISCUSSION

Synthesis and Characterization of the $FePcF_{16}$-rGO Hybrid. We report the successful synthesis of a novel nanohybrid material, integrating $FePcF_{16}$ and rGO, representing a significant advancement in the field. To synthesize $FePcF_{16}$, we employed a modified procedure reported by our research group where the cyclotetramerization of PnF_4 is achieved via a solid-state reaction.[35] Following an established procedure adapted to incorporate the unique properties of $FePcF_{16}$, the $FePcF_{16}$-rGO hybrid was prepared, as illustrated in Scheme 1.[43]

Figure 1A shows the FT-IR characterization that confirms the $FePcF_{16}$ and $FePcF_{16}$-rGO hybrid preparation. The absence of the C≡N vibration peak at 2246 cm^{-1} and the retention of the C−F at 1489 cm^{-1} indicate the formation of $FePcF_{16}$. rGO formation is evidenced by observing characteristic vibrational peaks at 3201 cm^{-1} (O−H) and 1581 cm^{-1} (C=C) in the FT-IR spectrum. These peaks are maintained during the synthesis of the $FePcF_{16}$-rGO hybrid, as seen in Figure 1B.

Absorption spectroscopy is a powerful tool for identifying different MPc complexes and understanding their electronic arrangement. Employing absorption spectroscopy enables us to determine the effect of switching the metal center or having different substituents on the different positions of the MPc. MPc complexes typically exhibit two characteristic bands in their absorption spectra: the Q-band (600 to 750 nm) and the B-band (300 to 450 nm). These bands provide valuable information about the electronic transitions within the Pc macrocycle; the Q-band generates from $\pi \rightarrow \pi^*$ transitions from orbitals a_{1u} to e_g^*, and the B-band generates from a_{2u} to e_g^*orbitals.[44] Figures S1 and S2 show the spectrum of the PnF_4 and the unsubstituted FePc compared with the $FePcF_{16}$, respectively. Figure S2 compares the unsubstituted FePc and $FePcF_{16}$, showing characteristic $\pi \rightarrow \pi^*$ transitions for the B-band at 322 and 316 nm, respectively, and Q-band transitions in the visible region at 654 and 660 nm, respectively. The Q-band of the $FePcF_{16}$ is red-shifted compared to the unsubstituted FePc, due to the substituents reducing the HOMO−LUMO energy gap of the phthalocyanine ring.[45] Figure 1C shows the UV−vis spectrum of the rGO, $FePcF_{16}$, and $FePcF_{16}$-rGO hybrid in DMSO (10^{-5} M). The lack of absorption peaks in the UV−vis spectrum of rGO in DMSO solution is likely due to poor dispersion of the rGO. $FePcF_{16}$ showed characteristic $\pi \rightarrow \pi^*$ transitions at 316 nm (B-band) and 660 nm (Q-band) in their absorption spectra. The $FePcF_{16}$-rGO hybrid exhibited similar transitions, with the B-band at 312 nm and the Q-band slightly red-shifted to 668 nm. The $FePcF_{16}$-rGO hybrid exhibits a red-shifted and broadened Q-band absorption (8 nm) compared to $FePcF_{16}$, signifying a charge transfer from $FePcF_{16}$ to rGO and a reduced HOMO−LUMO energy gap in the phthalocyanine ring due to $\pi - \pi$ interactions between Pc and rGO.[39]

Scheme 1. Schematic Illustrating the Synthesis of the $FePcF_{16}$-rGO Hybrid[a]

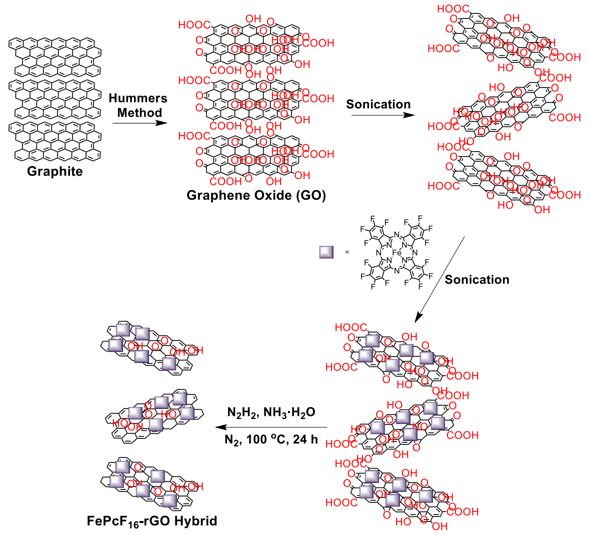

[a]The process involves oxidizing graphite to graphene oxide via a modified Hummers method, anchoring $FePcF_{16}$ onto the GO surface, and reducing it with hydrazine to form the final hybrid material.

Figure 1D showcases the Raman spectra for $FePcF_{16}$, rGO, and the $FePcF_{16}$-rGO hybrid. In the rGO spectrum, the signature G band (1579 cm^{-1}) arises from the in-plane vibration of sp^2 bonded carbon atoms, indicative of the ordered graphitic structure.[46] On the other hand, the D band (1341 cm^{-1}) originates from defects and disorder within the sp^2 network, such as vacancies, edges, or sp^3 hybridized carbon atoms.[47,48] In the hybrid spectrum, we observe a shift in both the G and D peaks compared to those in pure rGO, with the G band shifting by 7 cm^{-1} and the D band by 8 cm^{-1}. These shifts strongly suggest an electron transfer interaction between the $FePcF_{16}$ molecules and the rGO sheets, potentially

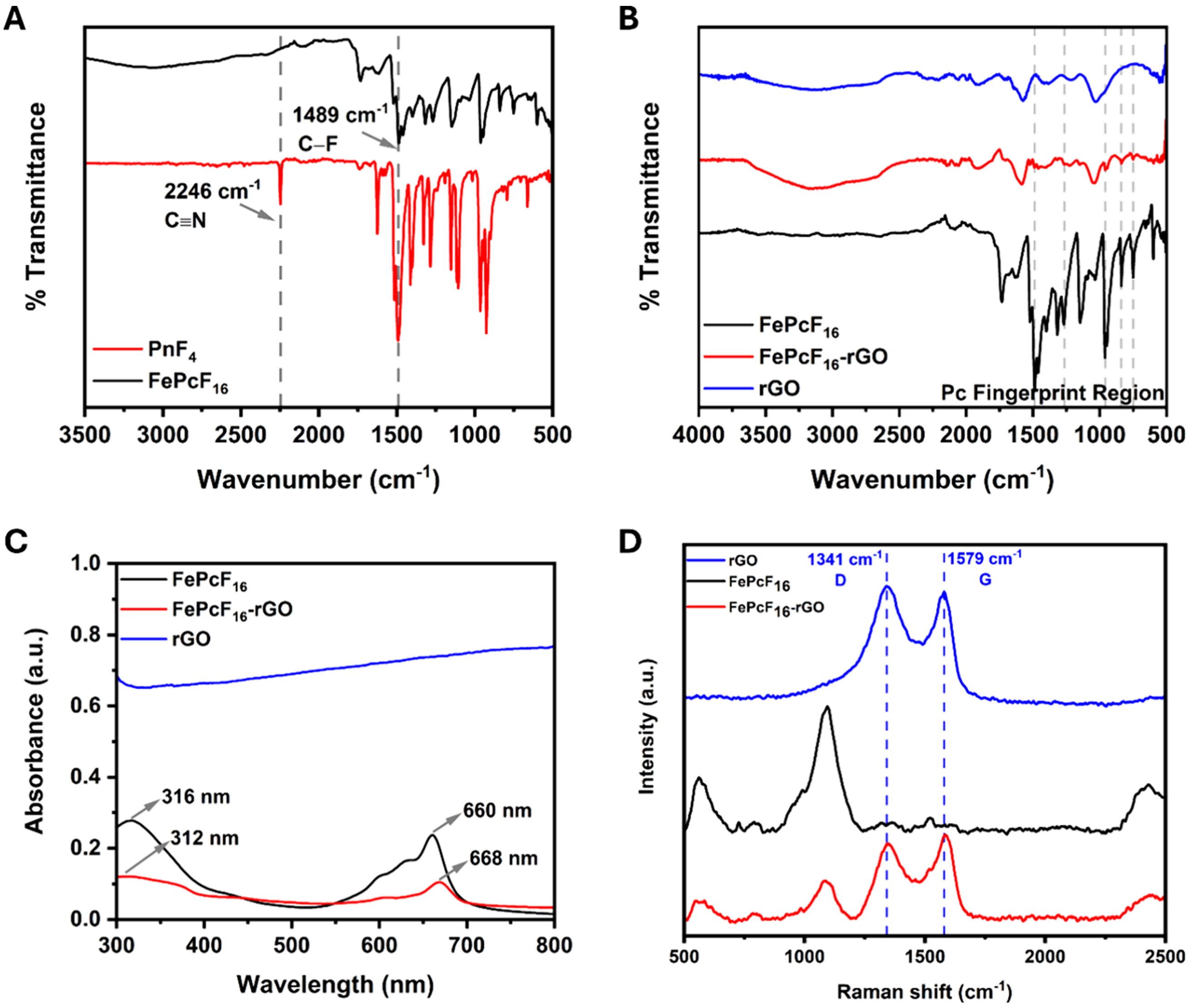

Figure 1. (A) FT-IR spectra of PnF_4 and $FePcF_{16}$. (B) FT-IR spectra of $FePcF_{16}$, rGO, and the $FePcF_{16}$-rGO hybrid. (C) UV–vis spectra of $FePcF_{16}$, rGO, and the $FePcF_{16}$-rGO hybrid in DMSO. (D) Raman spectra of $FePcF_{16}$, rGO, and the $FePcF_{16}$-rGO hybrid.

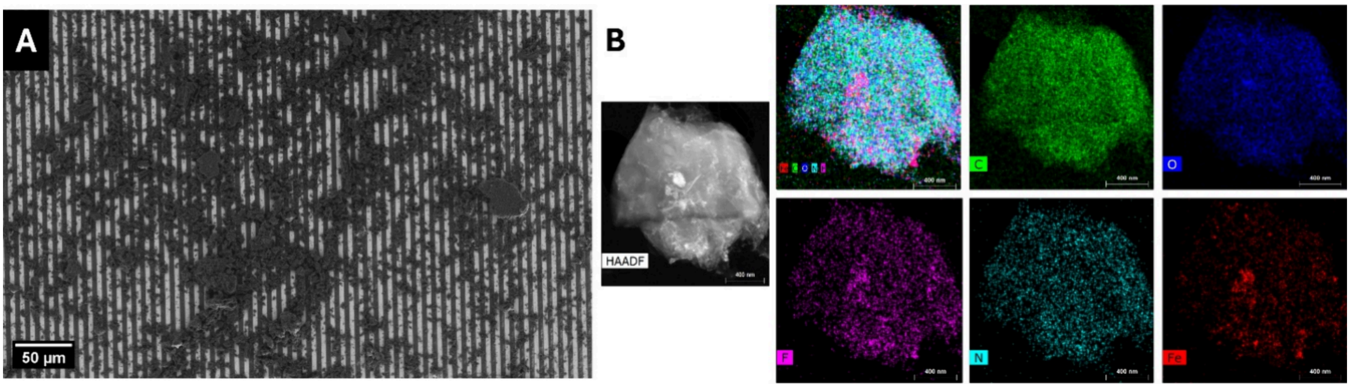

Figure 2. (A) SEM images of the IDE sensor based on the $FePcF_{16}$-rGO hybrid. (B) High-angle annular dark field (HAADF) scanning transmission electron microscopy (HAADF-STEM) image and EDS elemental mappings of the $FePcF_{16}$-rGO hybrid.

influencing the electronic properties and enhancing the sensitivity of the hybrid material for gas sensing applications.[49]

SEM analysis was employed to investigate the morphology and distribution of various materials across different electrode configurations. Figure 2A and Figure S3 showcase the uniform distribution of the $FePcF_{16}$-rGO hybrid across an interdigitated electrode and powder form, respectively. This well-dispersed network facilitates efficient electron transport and gas diffusion and maximizes the exposure of active sites, contributing to improved sensing performance. Moreover, TEM analysis of the

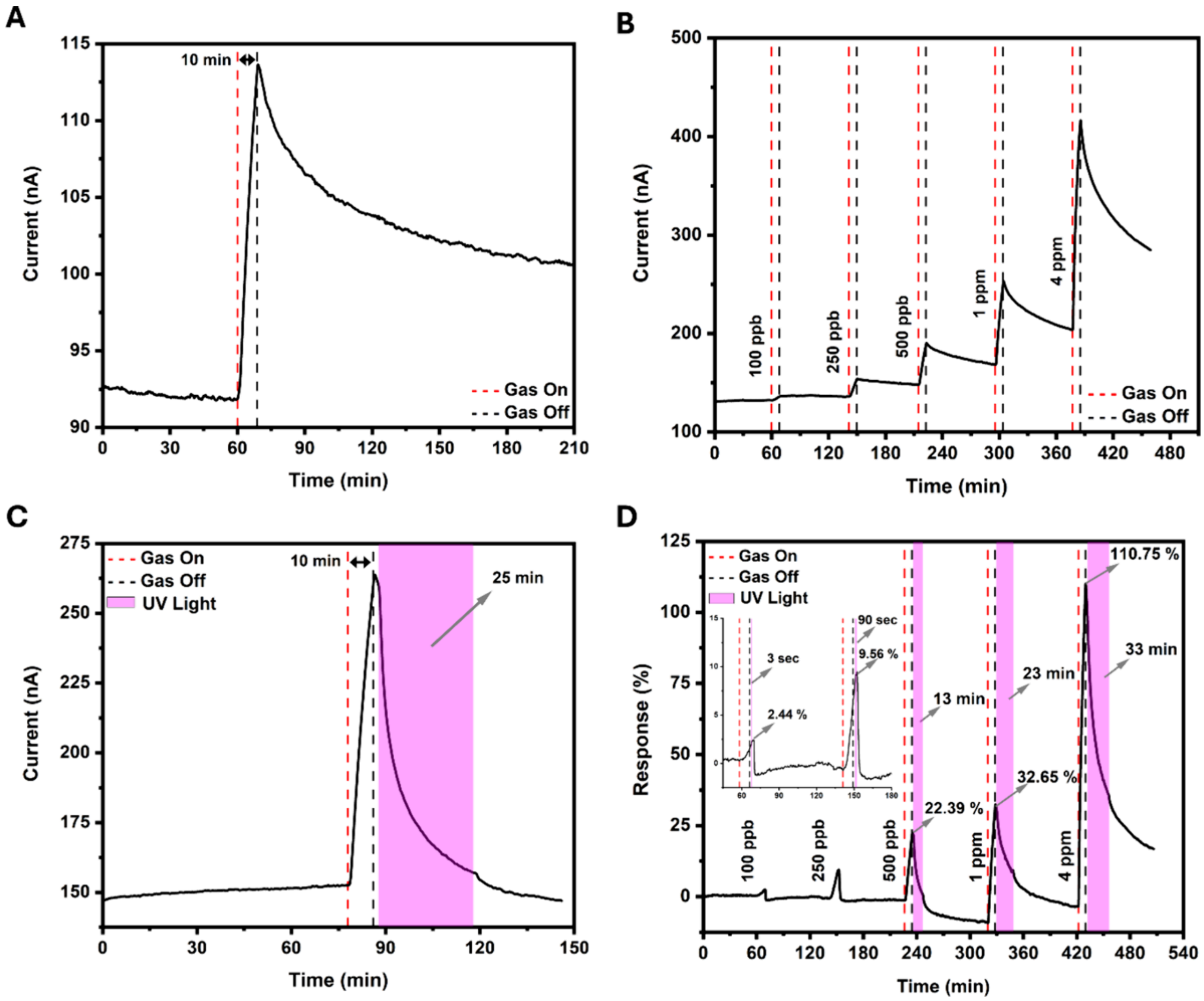

Figure 3. (A) Dynamic current characteristic curve of the $FePcF_{16}$-rGO hybrid sensor exposed to 500 ppb NO_2 (without UV irradiation). (B) Dynamic current characteristic curve of the $FePcF_{16}$-rGO hybrid sensor exposed to different concentrations of NO_2 (0.1, 0.25, 0.5, 1.0, and 4 ppm) without UV irradiation. (C) Dynamic current characteristic curve of the $FePcF_{16}$-rGO hybrid sensor exposed to 1 ppm NO_2 (recovered with UV irradiation). (D) Dynamic response characteristic curve of the $FePcF_{16}$-rGO hybrid sensor exposed to different concentrations of NO_2 (0.1, 0.25, 0.5, 1.0, and 4 ppm) with UV irradiation recovery.

$FePcF_{16}$-rGO hybrid shows a highly interconnected structure where the $FePcF_{16}$ are homogeneously dispersed on the rGO sheets. High-resolution TEM images in Figure S4 confirm the nanoscale interaction between $FePcF_{16}$ and rGO, hence the intimate contact for efficient charge transfer.

Energy-dispersive X-ray spectroscopy (EDS) analysis confirmed the presence of $FePcF_{16}$ in the rGO hybrid powder (Figure S5 and Table S1). The elemental composition of $FePcF_{16}$-rGO hybrid was determined to be mass% values of N (21.16085%), O (36.73014%), Fe (24.68725%), and F (17.42176%). The presence of Fe, N, and F confirms the successful synthesis of the hybrid material. The carbon percentage was not included in the analysis because the base of the TEM support grid consists of a copper and carbon base that contributes a lot to the detected carbon signal. Therefore, it is not easy to give the exact amount of carbon coming from the sample due to the overwhelming contribution of the grid. Elemental mapping, as shown in Figure 2B, further corroborates the distribution of these elements within the hybrid material.

Gas Sensing Properties of the $FePcF_{16}$-rGO Hybrid. The gold IDEs (ED-IDE3-Au) are obtained from MicruX Technologies with the following features: the gap between digits is 5 μm, and the number of digits is 180 pairs with a width of 5 μm. $FePcF_{16}$-rGO is deposited onto IDEs using a drop-coating method to fabricate a chemiresitive gas sensor. The $FePcF_{16}$-rGO hybrid is dispersed in ethanol by sonication treatment. The dispersed material is then drop-cast onto the IDE surface using the drop-casting technique and dried to form the film that connects the IDE pairs. The SEM image (Figure 2A) shows a close-up view of $FePcF_{16}$-rGO materials deposited on the substrate, forming continuous pathways bridging the IDE. The gas sensing experiments were conducted within a controlled environment using the gas sensing system illustrated in Figure S6. Before gas testing, the device's functionality was verified by obtaining its I−V curves under a bias voltage. The device is connected, and compressed N_2 gas is injected into the chamber and purged for 10 min to ensure consistent signal output from the devices. The results are shown in Figure S7 by applying voltages between +7 V and −7

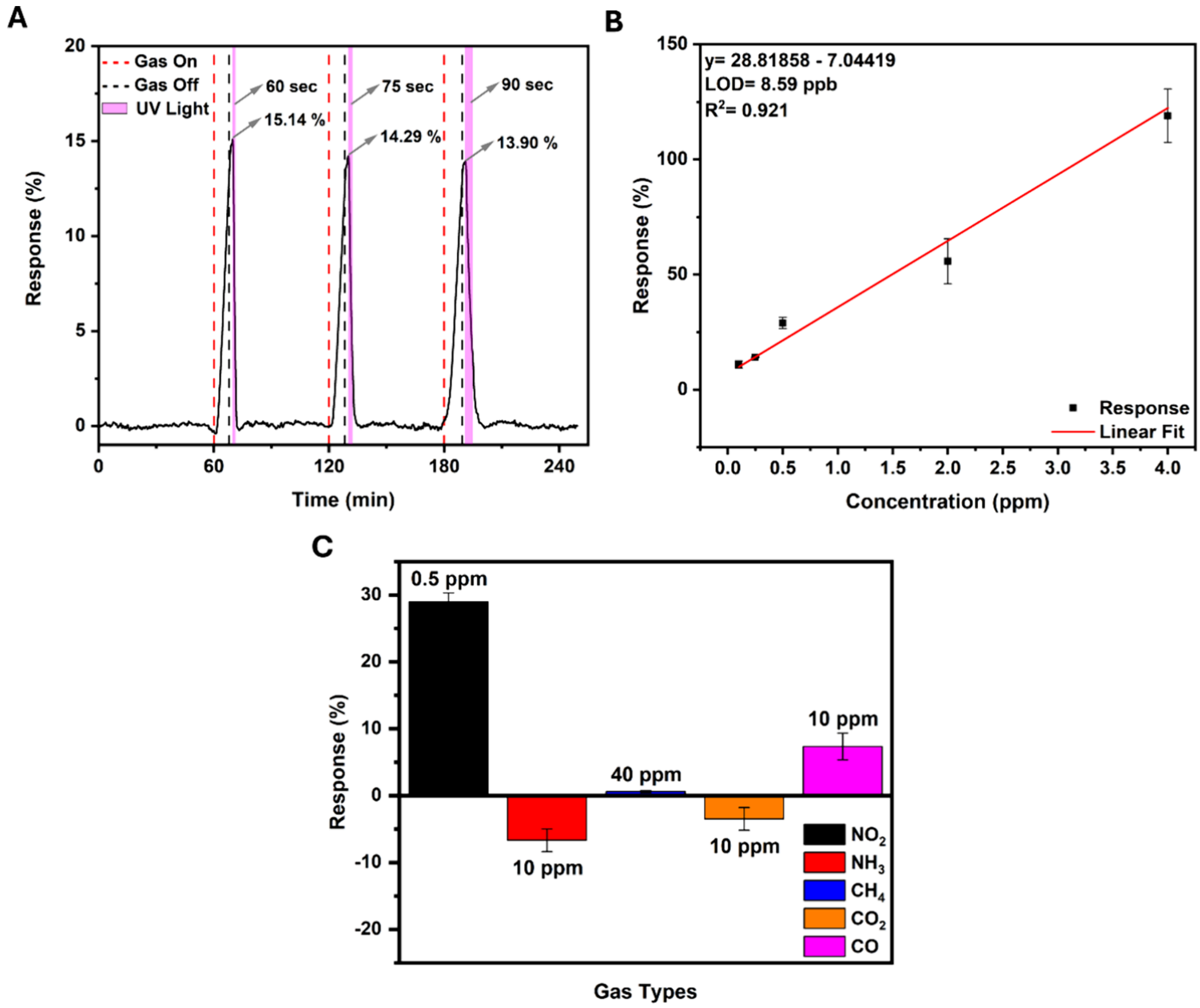

Figure 4. (A) Dynamic response characteristic curve of the FePcF$_{16}$-rGO hybrid sensor exposed to three cycles of 100 ppb NO$_2$. (B) Linear fit of the response of the FePcF$_{16}$-rGO hybrid sensor to the concentration NO$_2$. (C) Response of FePcF$_{16}$-rGO hybrid-based sensor to NO$_2$ and other gases.

V, exhibiting a nonlinear (semiconductor) behavior of the I−V curve of FePcF$_{16}$-rGO hybrid on the IDE.

The gas sensing properties of the FePcF$_{16}$-rGO hybrid were evaluated using NO$_2$ as the target gas and diluted with N$_2$. The characteristic dynamic response curves of sensing devices utilizing FePcF$_{16}$ and rGO when exposed electrical conductivity compared to its FePcF$_{16}$ counterpart, aligning with the I−V curve test findings. Both the FePcF$_{16}$-based sensor and the rGO sensor exhibited responsiveness to NO$_2$. However, it is essential to note that neither material could recover after the initial detection cycle, indicating they are susceptible to poisoning, which aligns with the reported literature.[50] In contrast, the FePcF$_{16}$-rGO hybrid gas sensor, as illustrated in Figure S5, demonstrates superior performance with enhanced response and recovery compared to its individual components.

The exposure time of the NO$_2$ gas was fixed at 10 min to facilitate comparative sensing experiments. In Figure 3A, we can observe that the FePcF$_{16}$-rGO hybrid gas sensor responds well to 500 ppb NO$_2$. The device demonstrated p-type semiconductor characteristics, wherein the sensor's current increased upon exposure to oxidizing gas NO$_2$ and subsequently recovered in N$_2$ despite the hybrid composition involving n-type (FePcF$_{16}$) and p-type (rGO) materials.[51] In Figure 3B, the sensor could sense different concentrations of NO$_2$ from 100 ppb to 4 ppm. However, the sensor will not recover independently after >120 min in N$_2$. UV light addressed the recovery issue observed in the gas sensors. Leveraging the photosensitivity properties of phthalocyanine, UV illumination significantly improved the recovery performance of the FePcF$_{16}$-rGO hybrid sensor.[52,53] The recovery time of the FePcF$_{16}$-rGO hybrid sensor was investigated upon UV light activation. After the NO$_2$ exposure, the gas flow was switched off, and the UV light was turned on 1 min after stopping the NO$_2$ flow to stabilize the sensor before switching on the UV-assisted recovery process. The recovery time was the time it took the sensor signal to achieve a steady state after the UV light was turned on. As expected, illuminating the FePcF$_{16}$-rGO hybrid increased its carrier concentration, enhanced conductivity, and achieved a gas desorption effect.[54] As shown in Figure 3C, the FePcF$_{16}$-rGO hybrid sensor exhibits significant recovery after exposure to NO$_2$ (1 ppm), with the current increasing due to the p-type semiconductor properties mentioned previously and recovering upon UV irradiation. In Figure 3D, the FePcF$_{16}$-rGO hybrid sensor was exposed to 0.1, 0.25, 0.5, 1, and 4 ppm NO_2. The sensor demonstrated a remarkable response to the different concentrations of NO_2, with values of 2.44, 9.56, 22.39, 32.65, and 110.75%, respectively. In addition, each of the concentrations recovered when exposed to UV irradiation due to the previously mentioned statement. Recovery, facilitated by UV irradiation, varied with concentration, ranging from 0.05 to 33 min, as shown in Table S2.

Reproducibility is a crucial aspect of gas sensor evaluation. To assess the sensor's reliability in detecting NO_2, we exposed it to a known concentration of NO_2 of 100 ppb for multiple cycles. This repetitive testing allowed us to consistently analyze the sensor's ability to detect the gas across exposures. We monitored the sensor's response (signal change) and recovery time between exposures to evaluate its performance. As mentioned, the same exposure and recovery procedure was repeated to evaluate the sensor's reusability. Figure 4A shows the sensor's response across three cycles, with 15.14, 14.29, and 13.90% values, indicating a stable and reproducible performance. This reproducible response at the ppb NO_2 level highlights the sensor's potential for practical applications due to its reusability.

Additionally, a linear fit of the response data is used to determine the theoretical limit of detection (LOD) for NO_2. The LOD refers to the minimum concentration of an analyte within a sensing element that can be reliably detected with a specified probability. Each response was measured three times to obtain an average, ensuring reliability and accuracy. The determination of LOD is given by eqs 3 and 4:[55,56]

$$\mathrm{RMS_{noise}} = \sqrt{\frac{S^2}{N}} = 0.08254 \tag{3}$$

$$\mathrm{LOD\ (ppm)} = 3 \times \frac{\mathrm{RMS_{noise}}}{\mathrm{slope}} = 8.59\ \mathrm{ppb} \tag{4}$$

RMS_{noise} is the root-mean-square-standard deviation of the noise, which is calculated to be equal to 0.08254 based on 290 data points (N) and a standard deviation (S) of 1.40562 from the baseline of the curve for the $FePcF_{16}$-rGO hybrid sensor, fitting to eq 3. Derived from the calculated RMS_{noise}, the theoretical limit of detection (LOD) for the $FePcF_{16}$-rGO hybrid sensor is determined to be 8.59 ppb (Figure 4B) at a signal-to-noise ratio of 3, as per eq 4.

Further study of our device was done by exposing the sensor to various gases to test its selectivity, which is a significant characteristic of gas sensors. The selectivity of our gas sensor was determined by exposing the device individually to other types of gases NH_3, methane (CH_4), carbon dioxide (CO_2), and carbon monoxide (CO)-at room temperature, as shown in Figure 4C. The reproducibility of the results was checked by testing each gas individually three times. The $FePcF_{16}$-rGO hybrid sensor exhibited good selectivity toward 0.5 ppm NO_2 at 28.9%. The device did not show significant responses to NH_3 and CO_2 at low concentrations, proving its ability to distinguish NO_2 from these potential interferents. In the case of NH_3 and CO_2, the response was negative since the device is a p-type semiconductor, and the current will decrease in the case of exposure to a reducing gas. However, the device showed a −6.7 and −3.5% response, respectively, only at higher concentrations. For CH_4 and CO, the response was sluggish even at higher concentrations, showing a response of 0.6 and 7.3%, respectively. Compared to other reported NO_2 sensors, especially those based on similar materials, as shown in Table S3, the $FePcF_{16}$-rGO sensor exhibits competitive performance. Although some sensors show higher sensitivity or lower detection limits, the $FePcF_{16}$-rGO hybrid sensor demonstrates a balanced combination of high response, a low theoretical detection limit (8.59 ppb), and recovery under UV light-assisted operation. This combination makes it a promising candidate for practical NO_2 detection applications, particularly where fast response and recovery times are required. This indicates that the $FePcF_{16}$-rGO sensor has higher selectivity for NO_2 at lower concentrations, which gives a strong and distinguishable response even at low levels of NO_2, while it only slightly responds to other gases even when their concentrations are increased.

Gas Sensing Mechanism. The $FePcF_{16}$-rGO hybrid sensor exhibits remarkable gas sensing capabilities due to the enhanced functionality of the combination of $FePcF_{16}$ and rGO, facilitating complementary interactions with target gas molecules. Additionally, the $FePcF_{16}$-rGO hybrid's p-type behavior stems from the interplay between the p-type semiconductor characteristics of rGO and the n-type semiconductor characteristics of $FePcF_{16}$.[35,50] The role of rGO in changing the electronic properties of the material toward improved conductivity and enhanced interactions with NO_2 molecules has been proven in similar materials to be the result of a combination of multiple factors, such as (i) restoration of conductive network from the removed oxygen-containing groups, regenerating the sp^2-bonded carbon network, (ii) allowing electron mobility, and (iii) providing high surface area for contact with gas molecules, thus improving interfacial interactions.[57−59] This unique combination of properties and interactions suggests that the gas sensing goes as follows:

The sensor's pre-exposure to atmospheric oxygen during fabrication leads to both physical and chemical adsorption of oxygen molecules onto the surface of the hybrid (eq 5)[60,61]

$$O_2(\mathrm{gas}) + e^- \rightarrow O\ _2(\mathrm{ads}) \tag{5}$$

The preadsorbed oxygen molecules can withdraw electrons from the hybrid surface, inducing a slight p-type character in the rGO. The following reaction processes can represent this electron transfer:

$$O_2(\mathrm{ads}) + e^- \rightarrow O_2^-(\mathrm{ads}) \tag{6}$$

$$O_2^-(\mathrm{ads}) + e^- \rightarrow 2O^-(\mathrm{ads}) \tag{7}$$

$$O^-(\mathrm{ads}) + e^- \rightarrow O^{2-}(\mathrm{ads}) \tag{8}$$

As the sensor encounters NO_2 gas, the interaction between the gas molecules and the preadsorbed oxygen species on the p-type hybrid layer triggers a complex series of electron transfer reactions (shown in eqs 9 and 10).[62,63] These reactions involve NO_2 trapping electrons from both the hybrid material and the preadsorbed oxygen species. This electron transfer process increases the concentration of holes (majority carriers in p-type material) within the rGO, leading to a rise in the sensor's conductivity.[64]

$$NO_2(\mathrm{gas}) + e^- \rightarrow NO_2^-(\mathrm{ads}) \tag{9}$$

$$NO_2(\mathrm{gas}) + O_2^- + 2e^- \rightarrow NO_2^-(\mathrm{ads}) + 2O^- \tag{10}$$

After the NO_2 flow is stopped and the remaining gas is purged from the sensing environment, the hybrid sensor is irradiated with UV light. This process takes advantage of the

$FePcF_{16}$'s photosensitivity and photogenerated electron−hole pairs within the material (eq 11)[65]

$$h\nu(\mathrm{UV}) \rightarrow \mathrm{h}^{+}(\mathrm{UV}) + \mathrm{e}^{-}(\mathrm{UV}) \tag{11}$$

During UV-aided recovery, photogenerated carriers facilitate the desorption of remaining NO_2 from the sensor surface, restoring its baseline conductivity.[66] One potential mechanism involves recombining photogenerated holes with the adsorbed NO_2 molecules, leading to their neutralization and subsequent desorption (eq 12).[67,68]

$$\mathrm{NO}_2^{-}(\mathrm{ads}) + \mathrm{h}^{+} \rightarrow \mathrm{NO}_2(\mathrm{gas}) \tag{12}$$

Furthermore, the UV photosensitivity of $FePcF_{16}$ allows for sensor recovery, with hole recombination potentially playing a significant role in the desorption of NO_2, ultimately restoring the baseline conductivity.

CONCLUSIONS

In conclusion, the $FePcF_{16}$-rGO hybrids were effectively synthesized through noncovalent interactions, where the $FePcF_{16}$ is functionalized on the surface of the rGO. This preserves the structural integrity and surface area of rGO and provides active sites for NO_2 adsorption by $FePcF_{16}$. The unique large-surface-area structure facilitated NO_2 diffusion, coupled with abundant active sites for NO_2 adsorption and excellent conductivity for efficient electron transport. As a result, the sensors exhibited remarkable sensitivity and linear response-concentration characteristics toward NO_2 at ambient temperature. UV light irradiation effectively addressed recovery issues in the sensors, offering a practical solution for improved performance. Notably, the $FePcF_{16}$-rGO hybrid sensor shows remarkable sensitivity toward low concentrations of NO_2 with a 15.14% response for 100 ppb and a quick recovery time when irradiated with UV light of 60 s. Moreover, our investigation into the sensor's selectivity revealed its robust response to NO_2 while maintaining minimal interference from other gases and can reach an LOD of 8.59 ppb NO_2.

The outstanding gas sensing response of the $FePcF_{16}$-rGO hybrid sensor originates from the complementary interactions between the composite material and target gas molecules, enabled by the synergistic effects of $FePcF_{16}$ and rGO. Additionally, the $FePcF_{16}$-rGO hybrid's p-type behavior stems from the interplay between the p-type semiconductor characteristics of rGO and the n-type semiconductor characteristics of $FePcF_{16}$. This unique combination suggests a complex gas sensing mechanism involving oxygen adsorption, electron transfer reactions with NO_2, and UV-aided desorption.

ASSOCIATED CONTENT

Supporting Information

The Supporting Information is available free of charge at https://pubs.acs.org/doi/10.1021/acsomega.4c08662.

> Additional UV−vis spectra, SEM and HRTEM images, and HAADF-STEM image and EDS analysis of the materials used in the sensor fabrication; normalized quantitative weight percentages for the elements in $FePcF_{16}$-rGO hybrid; schematic illustration of the gas sensing facility; characterization of the ohmic behavior of the gas sensor; dynamic response curves of the device; summary tables of the response and recovery times and sensor comparison (PDF)

AUTHOR INFORMATION

Corresponding Author

Dalice M. Piñero Cruz − *Faculty of Natural Sciences, University of Puerto Rico, Río Piedras Campus, San Juan 00931, Puerto Rico; Molecular Science Research Center, San Juan 00926-2614, Puerto Rico;* orcid.org/0000-0001-6331-761X; Email: dalice.pinero@upr.edu

Authors

John A. Cruz Lozada − *Faculty of Natural Sciences, University of Puerto Rico, Río Piedras Campus, San Juan 00931, Puerto Rico; Molecular Science Research Center, San Juan 00926-2614, Puerto Rico*

Ricardo A. Rosario − *Faculty of Natural Sciences, University of Puerto Rico, Río Piedras Campus, San Juan 00931, Puerto Rico*

Soraya Y. Flores − *Faculty of Natural Sciences, University of Puerto Rico, Río Piedras Campus, San Juan 00931, Puerto Rico*

Kim Kisslinger − *Center for Functional Nanomaterials, Brookhaven National Laboratory, Upton, New York 11973-5000, United States*

Luis F. Fonseca − *Faculty of Natural Sciences, University of Puerto Rico, Río Piedras Campus, San Juan 00931, Puerto Rico;* orcid.org/0000-0001-5534-7202

Complete contact information is available at: https://pubs.acs.org/10.1021/acsomega.4c08662

Author Contributions

All authors have approved the final version of the manuscript. J.C.L.: conceptualization, methodology, investigation, formal analysis, experimentation, writing-original draft, and editing. R.R.H.: experimentation and methodology. S.Y.F.: methodology. K.K.: surfaces analysis TEM. L.F.F.: conceptualization, supervision, writing−review, editing, and funding acquisition. D.P.C.: conceptualization, supervision, writing−review and editing, and funding acquisition.

Funding

This work was supported by NSF-CREST CIRE2N (Grant Number HRD-1736093).

Notes

The authors declare no competing financial interest.

ACKNOWLEDGMENTS

This research used resources of the Center for Functional Nanomaterials (CFN), which is a U.S. Department of Energy Office of Science User Facility, at Brookhaven National Laboratory under Contract No. DESC0012704. The authors would like to acknowledge the Materials Characterization Center (MCC) of the University of Puerto Rico for use of research infrastructure and instrumentation.

REFERENCES

(1) Khan, M.; Rao, M.; Li, Q. Recent Advances in Electrochemical Sensors for Detecting Toxic Gases: NO2, SO2 and H2S. *Sensors* **2019**, *19* (4), 905.

(2) Mowry, C. D.; Jarek, R. L.; Román-Kustas, J.; Telles, A. C.; Pimentel, A. S. Gas Analysis by Mass Spectrometry. *Mater. Charact.* **2019**, 143−152.

(3) Shi, J.; Jiang, Y.; Duan, Z.; Li, J.; Yuan, Z.; Tai, H. Designing an Optical Gas Chamber with Stepped Structure for Non-Dispersive Infrared Methane Gas Sensor. *Sens. Actuators Phys.* **2024**, *367*, No. 115052.

(4) Kumar, A.; Prajesh, R. The Potential of Acoustic Wave Devices for Gas Sensing Applications. *Sens. Actuators Phys.* **2022**, *339*, No. 113498.

(5) Nazemi, H.; Joseph, A.; Park, J.; Emadi, A. Advanced Micro- and Nano-Gas Sensor Technology: A Review. *Sensors* **2019**, *19* (6), 1285.

(6) Li, Q.; Zeng, W.; Li, Y. Metal Oxide Gas Sensors for Detecting NO2 in Industrial Exhaust Gas: Recent Developments. *Sens. Actuators B Chem.* **2022**, *359*, No. 131579.

(7) Ramentol, E.; Grimm, S.; Stinzendörfer, M.; Wagner, A. Short-Term Air Pollution Forecasting Using Embeddings in Neural Networks. *Atmosphere* **2023**, *14* (2), 298.

(8) US Environmental Protection Agency *Nitrogen Dioxide's Impact on Indoor Air Quality*. https://www.epa.gov/indoor-air-quality-iaq/nitrogen-dioxides-impact-indoor-air-quality (accessed 2024−04−06).

(9) Hesterberg, T. W.; Bunn, W. B.; McClellan, R. O.; Hamade, A. K.; Long, C. M.; Valberg, P. A. Critical Review of the Human Data on Short-Term Nitrogen Dioxide (NO2) Exposures: Evidence for NO2 No-Effect Levels. *Crit. Rev. Toxicol.* **2009**, *39* (9), 743−781.

(10) Huang, W.; Zhuang, X.; Melkonyan, F. S.; Wang, B.; Zeng, L.; Wang, G.; Han, S.; Bedzyk, M. J.; Yu, J.; Marks, T. J.; Facchetti, A. UV−Ozone Interfacial Modification in Organic Transistors for High-Sensitivity NO $_2$ Detection. *Adv. Mater.* **2017**, *29* (31), No. 1701706.

(11) Pohanish, R. P. *Sittig's Handbook of Toxic and Hazardous Chemicals and Carcinogens*, Seventh ed.; William Andrew, Applied Science Publishers, 2019.

(12) Piedrahita, R.; Xiang, Y.; Masson, N.; Ortega, J.; Collier, A.; Jiang, Y.; Li, K.; Dick, R. P.; Lv, Q.; Hannigan, M.; Shang, L. The next Generation of Low-Cost Personal Air Quality Sensors for Quantitative Exposure Monitoring. *Atmospheric Meas. Technol.* **2014**, *7* (10), 3325−3336.

(13) Okechukwu, V. O.; Idris, A. O.; Umukoro, E. H.; Azizi, S.; Maaza, M. Exploring the Contribution of Intelligent Nanomaterials in Gas Sensing. *ChemistrySelect* **2024**, *9* (5), No. e202304703.

(14) Zhou, X.; Qi, M.; Li, K.; Xue, Z.; Wang, T. Gas Sensors Based on Nanoparticle-Assembled Interfaces and Their Application in Breath Detection of Lung Cancer. *Cell Rep. Phys. Sci.* **2023**, *4* (11), No. 101678.

(15) Wang, C.; Yin, L.; Zhang, L.; Xiang, D.; Gao, R. Metal Oxide Gas Sensors: Sensitivity and Influencing Factors. *Sensors* **2010**, *10* (3), 2088−2106.

(16) Sahu, P. K.; Pandey, R. K.; Dwivedi, R.; Mishra, V. N.; Prakash, R. Polymer/Graphene Oxide Nanocomposite Thin Film for NO2 Sensor: An in Situ Investigation of Electronic, Morphological, Structural, and Spectroscopic Properties. *Sci. Rep.* **2020**, *10* (1), 2981.

(17) Han, B.; Duan, Z.; Xu, J.; Zhu, Y.; Xu, Q.; Wang, H.; Tai, H.; Weng, J.; Zhao, Y. The Art of Integrated Functionalization: Super Stable Black Phosphorus Achieved through Metal-Organic Framework Coating. *Adv. Funct. Mater.* **2020**, *30* (27), No. 2002232.

(18) Sahu, P. K.; Chandra, L.; Pandey, R. K.; Mehta, N. S.; Dwivedi, R.; Mishra, V. N.; Prakash, R. Fast Development of Self-Assembled, Highly Oriented Polymer Thin Film and Observation of Dual Sensing Behavior of Thin Film Transistor for Ammonia Vapor. *Macromol. Chem. Phys.* **2019**, *220* (11), No. 1900010.

(19) Duan, X.; Duan, Z.; Zhang, Y.; Liu, B.; Li, X.; Zhao, Q.; Yuan, Z.; Jiang, Y.; Tai, H. Enhanced NH3 Sensing Performance of Polyaniline via a Facile Morphology Modification Strategy. *Sens. Actuators B Chem.* **2022**, *369*, No. 132302.

(20) Zhang, Y.; Li, Y.; Jiang, Y.; Duan, Z.; Yuan, Z.; Liu, B.; Huang, Q.; Zhao, Q.; Yang, Y.; Tai, H. Synergistic Effect of Charge Transfer and Interlayer Swelling in V2CTx/SnS2 Driving Ultrafast and Highly Sensitive NO2 Detection at Room Temperature. *Sens. Actuators B Chem.* **2024**, *411*, No. 135788.

(21) Zhang, Y.; Jiang, Y.; Yuan, Z.; Liu, B.; Zhao, Q.; Huang, Q.; Li, Z.; Zeng, W.; Duan, Z.; Tai, H. Synergistic Effect of Electron Scattering and Space Charge Transfer Enabled Unprecedented Room Temperature NO2 Sensing Response of SnO2. *Small* **2023**, *19* (48), No. 2303631.

(22) Zhao, Q.; Zhou, W.; Zhang, M.; Wang, Y.; Duan, Z.; Tan, C.; Liu, B.; Ouyang, F.; Yuan, Z.; Tai, H.; Jiang, Y. Edge-Enriched Mo$_2$TiC$_2$ T$_x$ /MoS$_2$ Heterostructure with Coupling Interface for Selective NO$_2$ Monitoring. *Adv. Funct. Mater.* **2022**, *32* (39), No. 2203528.

(23) Chang, Y.-S.; Chen, F.-K.; Tsai, D.-C.; Kuo, B.-H.; Shieu, F.-S. N-Doped Reduced Graphene Oxide for Room-Temperature NO Gas Sensors. *Sci. Rep.* **2021**, *11* (1), 20719.

(24) Kumar, R.; Kaur, A. Chemiresistive Gas Sensors Based on Thermally Reduced Graphene Oxide for Sensing Sulphur Dioxide at Room Temperature. *Diam. Relat. Mater.* **2020**, *109*, No. 108039.

(25) Schedin, F.; Geim, A. K.; Morozov, S. V.; Hill, E. W.; Blake, P.; Katsnelson, M. I.; Novoselov, K. S. Detection of Individual Gas Molecules Adsorbed on Graphene. *Nat. Mater.* **2007**, *6* (9), 652−655.

(26) Park, H. J.; Kim, W.-J.; Lee, H.-K.; Lee, D.-S.; Shin, J.-H.; Jun, Y.; Yun, Y. J. Highly Flexible, Mechanically Stable, and Sensitive NO2 Gas Sensors Based on Reduced Graphene Oxide Nanofibrous Mesh Fabric for Flexible Electronics. *Sens. Actuators B Chem.* **2018**, *257*, 846−852.

(27) Zhou, Y.; Lin, X.; Huang, Y.; Guo, Y.; Gao, C.; Xie, G.; Jiang, Y. Impact of Further Thermal Reduction on Few-Layer Reduced Graphene Oxide Film and Its n-p Transition for Gas Sensing. *Sens. Actuators B Chem.* **2016**, *235*, 241−250.

(28) Wang, X.; Gu, D.; Li, X.; Lin, S.; Zhao, S.; Rumyantseva, M. N.; Gaskov, A. M. Reduced Graphene Oxide Hybridized with WS2 Nanoflakes Based Heterojunctions for Selective Ammonia Sensors at Room Temperature. *Sens. Actuators B Chem.* **2019**, *282*, 290−299.

(29) Mao, S.; Cui, S.; Lu, G.; Yu, K.; Wen, Z.; Chen, J. Tuning Gas-Sensing Properties of Reduced Graphene Oxide Using Tin Oxide Nanocrystals. *J. Mater. Chem.* **2012**, *22* (22), 11009.

(30) Zhao, Y.; Li, X.; Zhou, X.; Zhang, Y. Review on the Graphene Based Optical Fiber Chemical and Biological Sensors. *Sens. Actuators B Chem.* **2016**, *231*, 324−340.

(31) Wang, B.; Wang, X.; Guo, Z.; Gai, S.; Li, Y.; Wu, Y. A Highly Sensitive Ppb-Level H $_2$ S Gas Sensor Based on Fluorophenoxy-Substituted Phthalocyanine Cobalt/rGO Hybrids at Room Temperature. *RSC Adv.* **2021**, *11* (11), 5993−6001.

(32) Gounden, D.; Nombona, N.; Van Zyl, W. E. Recent Advances in Phthalocyanines for Chemical Sensor, Non-Linear Optics (NLO) and Energy Storage Applications. *Coord. Chem. Rev.* **2020**, *420*, No. 213359.

(33) Klyamer, D. D.; Sukhikh, A. S.; Krasnov, P. O.; Gromilov, S. A.; Morozova, N. B.; Basova, T. V. Thin Films of Tetrafluorosubstituted Cobalt Phthalocyanine: Structure and Sensor Properties. *Appl. Surf. Sci.* **2016**, *372*, 79−86.

(34) Klyamer, D.; Sukhikh, A.; Gromilov, S.; Krasnov, P.; Basova, T. Fluorinated Metal Phthalocyanines: Interplay between Fluorination Degree, Films Orientation, and Ammonia Sensing Properties. *Sensors* **2018**, *18* (7), 2141.

(35) Flores, S. Y.; Gonzalez-Espiet, J.; Cintrón, J.; Villanueva, N. D. J.; Camino, F. E.; Kisslinger, K.; Cruz, D. M. P.; Rivera, R. D.; Fonseca, L. F. Fluorinated Iron and Cobalt Phthalocyanine Nanowire Chemiresistors for Environmental Gas Monitoring at Parts-per-Billion Levels. *ACS Appl. Nano Mater.* **2022**, *5* (4), 4688−4699.

(36) Kumar, A.; Samanta, S.; Singh, A.; Roy, M.; Singh, S.; Basu, S.; Chehimi, M. M.; Roy, K.; Ramgir, N.; Navaneethan, M.; Hayakawa, Y.; Debnath, A. K.; Aswal, D. K.; Gupta, S. K. Fast Response and High Sensitivity of ZnO Nanowires—Cobalt Phthalocyanine Heterojunction Based H $_2$ S Sensor. *ACS Appl. Mater. Interfaces* **2015**, *7* (32), 17713−17724.

(37) Prasongkit, J.; Tangsukworakhun, S.; Jaisutti, R.; Osotchan, T. Highly Sensitive and Selective Sensing of Acetone and Hydrogen Sulfide Using Metal Phthalocyanine − Carbon Nanotube Hybrids. *Appl. Surf. Sci.* **2020**, *532*, No. 147314.

(38) Saini, R.; Mahajan, A.; Bedi, R. K.; Aswal, D. K.; Debnath, A. K. Phthalocyanine Based Nanowires and Nanoflowers as Highly Sensitive Room Temperature Cl $_2$ Sensors. *RSC Adv.* **2014**, *4* (31), 15945.

(39) Guo, Z.; Wang, B.; Wang, X.; Li, Y.; Gai, S.; Wu, Y.; Cheng, X. A High-Sensitive Room Temperature Gas Sensor Based on Cobalt Phthalocyanines and Reduced Graphene Oxide Nanohybrids for the

Ppb-Levels of Ammonia Detection. *RSC Adv.* **2019**, *9* (64), 37518−37525.

(40) Kumar, S.; Kaur, N.; Sharma, A. K.; Mahajan, A.; Bedi, R. K. Improved Cl_2 Sensing Characteristics of Reduced Graphene Oxide When Decorated with Copper Phthalocyanine Nanoflowers. *RSC Adv.* **2017**, *7* (41), 25229−25236.

(41) Otero Vélez, C.; Flores, S. Y.; Fonseca, L. F.; Piñero Cruz, D. M. Palladium Phthalocyanine Nanowire-Based Highly Sensitive Sensors for NO2(g) Detection. *Sensors* **2024**, *24* (6), 1819.

(42) Yang, C.-M.; Chen, T.-C.; Yang, Y.-C.; Meyyappan, M. Annealing Effect on UV-Illuminated Recovery in Gas Response of Graphene-Based NO_2 Sensors. *RSC Adv.* **2019**, *9* (40), 23343−23351.

(43) Zhou, X.; Wang, X.; Wang, B.; Chen, Z.; He, C.; Wu, Y. Preparation, Characterization and NH3-Sensing Properties of Reduced Graphene Oxide/Copper Phthalocyanine Hybrid Material. *Sens. Actuators B Chem.* **2014**, *193*, 340−348.

(44) Ghani, F.; Kristen, J.; Riegler, H. Solubility Properties of Unsubstituted Metal Phthalocyanines in Different Types of Solvents. *J. Chem. Eng. Data* **2012**, *57* (2), 439−449.

(45) Günsel, A.; Bilgiçli, A. T.; Pişkin, H.; Çaylak Delibaş, N.; Yarasir, M. N.; Gündüz, B. Synthesis, Characterization, and Optical and Surface Properties of (4-(Trifluoromethylthio)Phenoxy) Copper-(II) Phthalocyanine. *New J. Chem.* **2018**, *42* (8), 6013−6022.

(46) Ferrari, A. C.; Meyer, J. C.; Scardaci, V.; Casiraghi, C.; Lazzeri, M.; Mauri, F.; Piscanec, S.; Jiang, D.; Novoselov, K. S.; Roth, S.; Geim, A. K. Raman Spectrum of Graphene and Graphene Layers. *Phys. Rev. Lett.* **2006**, *97* (18), No. 187401.

(47) Eckmann, A.; Felten, A.; Mishchenko, A.; Britnell, L.; Krupke, R.; Novoselov, K. S.; Casiraghi, C. Probing the Nature of Defects in Graphene by Raman Spectroscopy. *Nano Lett.* **2012**, *12* (8), 3925−3930.

(48) Cançado, L. G.; Jorio, A.; Ferreira, E. H. M.; Stavale, F.; Achete, C. A.; Capaz, R. B.; Moutinho, M. V. O.; Lombardo, A.; Kulmala, T. S.; Ferrari, A. C. Quantifying Defects in Graphene via Raman Spectroscopy at Different Excitation Energies. *Nano Lett.* **2011**, *11* (8), 3190−3196.

(49) Chunder, A.; Pal, T.; Khondaker, S. I.; Zhai, L. Reduced Graphene Oxide/Copper Phthalocyanine Composite and Its Optoelectrical Properties. *J. Phys. Chem. C* **2010**, *114* (35), 15129−15135.

(50) Lu, G.; Park, S.; Yu, K.; Ruoff, R. S.; Ocola, L. E.; Rosenmann, D.; Chen, J. Toward Practical Gas Sensing with Highly Reduced Graphene Oxide: A New Signal Processing Method To Circumvent Run-to-Run and Device-to-Device Variations. *ACS Nano* **2011**, *5* (2), 1154−1164.

(51) Liu, Y.; Xiao, S.; Du, K. Chemiresistive Gas Sensors Based on Hollow Heterojunction: A Review. *Adv. Mater. Interfaces* **2021**, *8* (12), No. 2002122.

(52) Fei, J.; Han, Z.; Deng, Y.; Wang, T.; Zhao, J.; Wang, C.; Zhao, X. Enhanced Photocatalytic Performance of Iron Phthalocyanine/TiO2 Heterostructure at Joint Fibrous Interfaces. *Colloids Surf. Physicochem. Eng. Asp.* **2021**, *625*, No. 126901.

(53) Musial, J.; Belet, A.; Mlynarczyk, D. T.; Kryjewski, M.; Goslinski, T.; Lambert, S. D.; Poelman, D.; Stanisz, B. J. Nanocomposites of Titanium Dioxide and Peripherally Substituted Phthalocyanines for the Photocatalytic Degradation of Sulfamethoxazole. *Nanomaterials* **2022**, *12* (19), 3279.

(54) Tomeček, D.; Piliai, L.; Hruška, M.; Fitl, P.; Gadenne, V.; Vorokhta, M.; Matolínová, I.; Vrňata, M. Study of Photoregeneration of Zinc Phthalocyanine Chemiresistor after Exposure to Nitrogen Dioxide. *Chemosensors* **2021**, *9* (9), 237.

(55) Song, Z.; Wei, Z.; Wang, B.; Luo, Z.; Xu, S.; Zhang, W.; Yu, H.; Li, M.; Huang, Z.; Zang, J.; Yi, F.; Liu, H. Sensitive Room-Temperature H_2S Gas Sensors Employing SnO_2 Quantum Wire/Reduced Graphene Oxide Nanocomposites. *Chem. Mater.* **2016**, *28* (4), 1205−1212.

(56) Li, M.; Zhou, D.; Zhao, J.; Zheng, Z.; He, J.; Hu, L.; Xia, Z.; Tang, J.; Liu, H. Resistive Gas Sensors Based on Colloidal Quantum Dot (CQD) Solids for Hydrogen Sulfide Detection. *Sens. Actuators B Chem.* **2015**, *217*, 198−201.

(57) Kholmanov, I. N.; Domingues, S. H.; Chou, H.; Wang, X.; Tan, C.; Kim, J.-Y.; Li, H.; Piner, R.; Zarbin, A. J. G.; Ruoff, R. S. Reduced Graphene Oxide/Copper Nanowire Hybrid Films as High-Performance Transparent Electrodes. *ACS Nano* **2013**, *7* (2), 1811−1816.

(58) Kholmanov, I. N.; Stoller, M. D.; Edgeworth, J.; Lee, W. H.; Li, H.; Lee, J.; Barnhart, C.; Potts, J. R.; Piner, R.; Akinwande, D.; Barrick, J. E.; Ruoff, R. S. Nanostructured Hybrid Transparent Conductive Films with Antibacterial Properties. *ACS Nano* **2012**, *6* (6), 5157−5163.

(59) Latif, U.; Dickert, F. Graphene Hybrid Materials in Gas Sensing Applications. *Sensors* **2015**, *15* (12), 30504−30524.

(60) Park, S.; An, S.; Mun, Y.; Lee, C. UV-Enhanced NO_2 Gas Sensing Properties of SnO_2-Core/ZnO-Shell Nanowires at Room Temperature. *ACS Appl. Mater. Interfaces* **2013**, *5* (10), 4285−4292.

(61) Yan, X.; Wu, Y.; Li, R.; Shi, C.; Moro, R.; Ma, Y.; Ma, L. High-Performance UV-Assisted NO_2 Sensor Based on Chemical Vapor Deposition Graphene at Room Temperature. *ACS Omega* **2019**, *4* (10), 14179−14187.

(62) Pisarkiewicz, T.; Maziarz, W.; Małolepszy, A.; Stobiński, L.; Michoń, D. A.; Szkudlarek, A.; Pisarek, M.; Kanak, J.; Rydosz, A. Nitrogen Dioxide Sensing Using Multilayer Structure of Reduced Graphene Oxide and α-Fe2O3. *Sensors* **2021**, *21* (3), 1011.

(63) Zhou, Y.; Gao, C.; Guo, Y. UV Assisted Ultrasensitive Trace NO_2 Gas Sensing Based on Few-Layer MoS_2 Nanosheet−ZnO Nanowire Heterojunctions at Room Temperature. *J. Mater. Chem. A* **2018**, *6* (22), 10286−10296.

(64) Drewniak, S.; Drewniak, Ł.; Pustelny, T. Mechanisms of NO2 Detection in Hybrid Structures Containing Reduced Graphene Oxide: A Review. *Sensors* **2022**, *22* (14), 5316.

(65) Chen, X.; Zeng, M.; Yang, J.; Hu, N.; Duan, X.; Cai, W.; Su, Y.; Yang, Z. Two-Dimensional Bimetallic Phthalocyanine Covalent-Organic-Framework-Based Chemiresistive Gas Sensor for Ppb-Level NO2 Detection. *Nanomaterials* **2023**, *13* (10), 1660.

(66) Jiang, W.; Wang, T.; Chen, X.; Li, B.; Zeng, M.; Hu, N.; Su, Y.; Zhou, Z.; Zhang, Y.; Yang, Z. Enhancing Room-Temperature NO_2 Detection of Cobalt Phthalocyanine Based Gas Sensor at an Ultralow Laser Exposure. *Phys. Chem. Chem. Phys.* **2020**, *22* (33), 18499−18506.

(67) Chizhov, A. S.; Rumyantseva, M. N.; Vasiliev, R. B.; Filatova, D. G.; Drozdov, K. A.; Krylov, I. V.; Abakumov, A. M.; Gaskov, A. M. Visible Light Activated Room Temperature Gas Sensors Based on Nanocrystalline ZnO Sensitized with CdSe Quantum Dots. *Sens. Actuators B Chem.* **2014**, *205*, 305−312.

(68) Tomeček, D.; Piliai, L.; Hruška, M.; Fitl, P.; Gadenne, V.; Vorokhta, M.; Matolínová, I.; Vrňata, M. Study of Photoregeneration of Zinc Phthalocyanine Chemiresistor after Exposure to Nitrogen Dioxide. *Chemosensors* **2021**, *9* (9), 237.